Analyzing the Accuracy of Fiber Tracking in Infiltrated Regions via Tumor Growth Simulation

Sebastiano Barbieri, Miriam H.A. Bauer, Jan Klein, Christopher Nimsky and Horst K. Hahn

Abstract—In this work, we present a model to simulate the growth of glioblastomas multiforma which takes into account both the varying volume of the tumor and its mechanical interaction with the brain parenchyma. Because these tumors grow preferentially along white matter fiber bundles, a tumor-invaded diffusion tensor field is simulated at the different stages of tumor development. This allows us to make a quantitative analysis about the error of fiber tracking algorithms in the presence of infiltrated tissue. Based upon the gained knowledge, we color code the segmentation of the glioma of a patient in order to visualize the uncertainty about regions containing important fiber bundles which fiber tracking algorithms may fail to reconstruct.

Index Terms—Tumor growth simulation, software phantom, fiber tracking, accuracy, PDE.

1 Introduction

Diffusion Tensor Imaging (DTI) models the anisotropic diffusion of water molecules as a 0-mean normal distribution, whose covariance matrix is given by the second order diffusion tensor [5, 29, 31]. In white matter we assume that the eigenvector associated with the largest eigenvalue of the tensor, i.e. the main diffusion direction, matches the direction of the underlying fiber bundles. Fiber tracking (FT) algorithms make use of this property to reconstruct neural pathways from the diffusion tensor field [4, 28, 30]. Since for patient data the true extent of fiber bundles is unknown, software or hardware phantoms represent an important tool to validate FT algorithms [13, 16, 27].

In this work we analyze the precision of FT algorithms in the presence of glioblastomas multiforma (GBM), the most common primary brain tumor in adults [32]. To this end, we make use of the DTI data of a healthy volunteer on which we simulate the growth of a tumor. We model both white matter infiltration and the deformation of brain parenchyma. This way, we are able to simulate the local displacement of fiber bundles caused by tumor expansion and compare the displaced fibers with others tracked on the basis of a tumor-invaded tensor field. Based on this analysis, we determine the characteristics of voxels in which FT algorithms may fail to reconstruct fibers of interest and visualize this uncertainty on patient data.

1.1 Related Work

Several approaches have been proposed to mathematically describe the growth of tumors, which may be subdivided according to the spatial scale they operate on. A first class of algorithms simulates tumor growth at the cellular level (cellular automata), whereas a second class of algorithms predicts the evolution of tumor density at a macroscopic scale, generally by making use of partial differential equations (PDEs). Although cellular automata approaches have been proposed for different tumors including GBMs (see [12, 19, 20, 21]) since we are interested in the macroscopic effects that tumor growth has on diffusion tensor imaging and not in the specific spatial ordering of tumor cells, we choose to focus on PDE based methods.

Among PDE based methods Li et al. [26] suggest a model that accounts for cell-proliferation and apoptosis. Cristini et al. [9] simulate the growth, neo-vascularization and infiltration of malignant gliomas. Clatz et al. [7] take into account both white matter infiltration and the mechanical deformation of the invaded structures. The patient's T1 and T2 images are registered to the Brainweb atlas [6] to take into account tissue properties and to a DTI atlas to take into account the preferential growth direction of GBMs along white matter fibers [32]. The approach subdivides the gross tumor volumes (GTVs, see [22]) into GTV1, the non-infiltrating component associated with volume increase and tissue deformation, and GTV2, the diffusion component associated with fast expansion and infiltration but smaller mass-effect.

We are especially interested in the effect of tumor growth on FT accuracy. In [3, 34] it has been shown using software phantoms that FT algorithms may consistently underestimate the spatial extent of fiber bundles with an error in the order of 5 mm. In [23] electrical stimulation was used in tumor patients to demonstrated that FT algorithms do not determine the correct size of fiber bundles. However, to the best of our knowledge, no quantitative analysis of FT accuracy in the presence of infiltrating tumors has been presented yet.

1.2 Contributions

The main contributions of this paper may be summarized as follows:

- We propose a novel tumor growth simulation model which couples two PDEs that describe the increase in tumor volume and the deformation of brain tissue
- We use patient specific DTI data and white and grey matter segmentations
- We realistically simulate the effect of tumor growth on the underlying DTI data
- We analyze the effect of infiltrated tissue on the precision of a deterministic FT algorithm
- Results of our analysis are used to color code the segmentation of the glioma of a patient, in order to determine areas which have a high risk of containing fibers which the FT algorithm may fail to reconstruct

2 Methods

Our method to simulate GBM growth is inspired by the work presented in [7], upon which we expand and propose a novel approach to coupling the PDEs that describe tumor invasion in the brain parenchyma and mechanical deformation of brain tissue (mass effect). Based on the T1 data of a healthy subject, we begin by segmenting the white and grey matter regions via a watershed-based algorithm [17]. Manual rigid registration is then used to align the T1 image and the segmented regions to the DTI data of the subject (specifically to the b0 image).

2.1 Tumor Growth Model

In order create the artificial tumor, we start by initializing the normalized tumor cell density function $c : \Omega \rightarrow [0, 1]$ where Ω is the image domain. This function may be used to compute the true cell density in

- *S. Barbieri (E-mail: sebastiano.barbieri@mevis.fraunhofer.de), J. Klein, and H.K. Hahn are with Fraunhofer MEVIS - Institute for Medical Image Computing, Universitätsallee 29, 28359 Bremen, Germany*
- *M.H.A. Bauer and Ch. Nimsky are with Department of Neurosurgery, University of Marburg, Baldingerstrasse, 35033 Marburg, Germany*

For information on obtaining reprints of this article, please send email to: tvcg@computer.org.

a voxel via multiplication with the carrying capacity constant $C_{\max}$, estimated to be approximately $3.5 \cdot 10^4$ cells/mm^3 [11, 35]. Given the center of the tumor x_0, we initialize c by computing

$$c(x) = \frac{1}{1+\|x-x_0\|^2} \tag{1}$$

where $\|\cdot\|$ is the euclidean norm.

While the tumor grows, the evolution of the density function c may be described via the sum of an anisotropic diffusion term which depends on the diffusivity of the underlying tissue and a cell proliferation term:

$$\frac{\partial c}{\partial t} = \underbrace{\operatorname{div}(D\nabla c)}_{\text{anisotropic diffusion}} + \underbrace{\rho c}_{\text{source term}} . \tag{2}$$

Here D is the diffusion tensor reconstructed at each voxel and ρ is a parameter which depends on the aggressiveness of the tumor. In our experiments we set $\rho = 0.77$/day, which leads to the simulation of a very quickly growing tumor.

Via a second PDE we model the mechanical deformation of brain tissue caused by tumor growth:

$$\operatorname{div}(\sigma) - \gamma \nabla c = 0 \tag{3}$$

where σ is the stress tensor and γ is a scaling factor for the pressure applied on the tissue by the growing tumor. The deformation force acts in the direction opposite to the gradient of the tumor density function. The stress tensor σ depends on the local displacement $u : \Omega \to \mathbb{R}^3$ and on the tissue dependent Lamé parameters λ and μ. In the brain regions where we allow for tissue displacement, i.e. white and grey matter, we use $\lambda = 991.43$ Pa and $\mu = 247.86$ Pa, which may be normalized to $\lambda = 1.0$ Pa and $\mu = 0.25$ Pa. The coupling factor γ is set to 1.0. We do not explicitly compute σ but solve instead the elastostatic equation, i.e. we find u such that all forces acting on the brain tissue sum up to zero. Assuming the tissue to be locally isotropic (the deformation magnitude does not depend on the direction of the applied force) and homogeneous the equilibrium equations may be explicitly derived [33]:

$$\begin{aligned}
0 &= (\lambda+\mu)(u_{1_{xx}} + u_{2_{xy}} + u_{3_{xz}}) + \mu(u_{1_{xx}} + u_{1_{yy}} + u_{1_{zz}}) - \gamma c_x \\
0 &= (\lambda+\mu)(u_{1_{xy}} + u_{2_{yy}} + u_{3_{yz}}) + \mu(u_{2_{xx}} + u_{2_{yy}} + u_{2_{zz}}) - \gamma c_y \\
0 &= (\lambda+\mu)(u_{1_{xz}} + u_{2_{yz}} + u_{3_{zz}}) + \mu(u_{3_{xx}} + u_{3_{yy}} + u_{3_{zz}}) - \gamma c_z
\end{aligned} \tag{4}$$

which may also be expressed in vector notation as

$$0 = (\lambda+\mu)\nabla(\nabla\cdot u) + \mu\nabla^2 u - \gamma\nabla c . \tag{5}$$

After introducing an artificial time variable T, Eq. 5 may be solved as the steady state in time of

$$\frac{\partial u}{\partial T} = (\lambda+\mu)\nabla(\nabla\cdot u) + \mu\nabla^2 u - \gamma\nabla c . \tag{6}$$

2.2 PDE Coupling and Discretization

We thus need to solve the coupled PDEs 2 and 6 with c and u set to 0 at the boundary of white and grey matter. We do this by approximating each partial derivative via finite differences and by employing an explicit gradient descent algorithm. For example, the time derivative in Eq. 2 will be approximated via

$$\frac{c^{i+1} - c^i}{\Delta t} = \operatorname{div}(D\nabla c) + \rho c \tag{7}$$

where i indicates the iteration number and Δt is the time step (we use $\Delta t = 0.2$ days). This leads to the iterative scheme

$$c^{i+1} = c^i + \Delta t \cdot (\operatorname{div}(D\nabla c) + \rho c) . \tag{8}$$

Equation 6 is solved analogously. In order to couple the two PDEs after each update to the tumor cell density function c we iteratively solve Eq. 6 to find the resulting displacement field and apply it to the diffusion tensor image. While doing this, we need to not only shift the single diffusion tensors according to u but also to appropriately reorient the main diffusion directions. The local transformation at position x is given by J_{x+u}, the Jacobi matrix of $x+u(x)$. The new tensor D^{i+1} at position $x+u(x)$ is then computed via

$$D^{i+1}(x+u(x)) = J_{x+u}\, D^i(x)\, J_{x+u}^{-1} . \tag{9}$$

This way, both the rotation and shearing of tensors are taken into account. However, in our experiments, considering only the rotational component of J_{x+u} led to results appearing visually more realistic. We therefore approximate J_{x+u} by means of the orthonormal matrix Q obtained via its QR decomposition [14, 15, 25] and J_{x+u}^{-1} via the transpose of Q.

In Fig. 1 we present an illustrative example of the need for tensor reorientation in 2D. Consider applying the displacement field

$$u(x) = \begin{pmatrix} x_1\cos\theta - x_2\sin\theta - x_1 \\ x_1\sin\theta + x_2\cos\theta - x_2 \end{pmatrix} \tag{10}$$

(which correspond to a global counterclockwise rotation by an angle θ) to the tensor schematized in Fig. 1(a). Simply shifting the center of the tensor leads to the configuration depicted in Fig. 1(b). Finally, since

$$J_{x+u} = \begin{pmatrix} \cos\theta & -\sin\theta \\ \sin\theta & \cos\theta \end{pmatrix} , \tag{11}$$

we rotate D according to Eq. 9 and obtain the result displayed in Fig. 1(c).

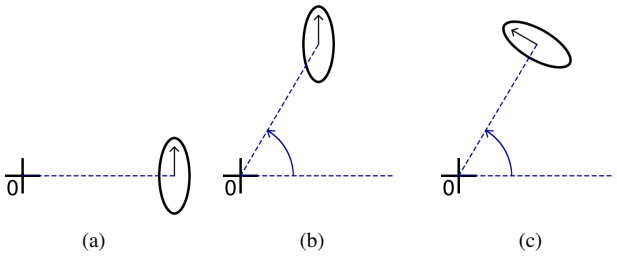

Fig. 1. (a) Schematic initial tensor configuration. (b) Application of the displacement field to the tensor without reorientation of the main diffusion direction. (c) Reorientation of the tensor by means of the Jacobi matrix.

Once we have applied the displacement field to the diffusion tensors and reoriented them, many tensors will likely not be centered on the image grid and we therefore need to solve a scattered data interpolation problem [1, 10]. For each voxel, we consider the set of displaced tensors $\{D_j\}$ with a distance d_j from the center x_o of the voxel which is smaller than a predefined radius R. Each of these tensors is then weighted according to an inverse square (Shepard) weighting function:

$$w(d_j;R) = \left(\frac{1}{d_j} - \frac{1}{R}\right)^2 \tag{12}$$

In our experiments R is initially chosen to be slightly smaller than the edge of a voxel but is arbitrarily increased if no displaced tensors are found. The interpolated tensor is computed via Log-Euclidean interpolation [2]:

$$D(x_o) = \exp\left(\frac{\sum_j w(d_j;R)\log(D_j)}{\sum_j w(d_j;R)}\right) \tag{13}$$

where exp and log indicate the matrix exponential and logarithm, respectively. Finally, if the tumor cell density $c(x_o)$ at the voxel x_o is positive, we additionally interpolate $D(x_o)$ with an isotropic tensor which models the diffusivity inside the tumor. Based on measurements on patient data, we set the eigenvalues of the isotropic tensor equal to 0.001 mm^2/s. For the interpolation, the isotropic tensor is weighted by $c(x_o)$ whereas $D(x_o)$ is weighted by $1 - c(x_o)$.

2.3 Summary of the Tumor Growth Algorithm

In this section, we briefly summarize how we solve the PDEs which simultaneously describe the tumor invasion in the brain parenchyma and its mechanical deformation.

{**Algorithm Start**}
Initialize c according to Eq. 1
for $i = 1$: fixed number of iterations **do**
  Update c according to Eq. 2
  repeat
    Update u according to Eq. 6 via an explicit gradient descent algorithm
  until $\|u^{k+1} - u^k\| < \varepsilon$
  Apply the displacement field to the tensor data and reorient according to Eq. 9
  Interpolate the tensor data on the image grid according to Eq. 13
  Interpolate with an isotropic tensor in voxels where c is positive
end for
{**Algorithm End**}

To reduce numerical errors, one may also keep track of the displacement fields computed for each c^i and apply their sum to the original tensor data instead of iteratively applying them to the tensor field.

2.4 Uncertainty Analysis

In order to analyze how tumor growth affects the accuracy of fiber tracking we start by simulating different stages of tumor growth on the DTI data of a healthy subject. At each time-point i, we perform the tracking of a specific fiber bundle near the lesion, based on the modified DTI data and obtain a set of fiber bundles $\{F_i\}$. In our experiments we use whole-brain fiber-tracking [8] and select the fibers that go through regions of interest. The whole-brain tracking approach is chosen for its superior reconstruction capabilities, see for example [24]. Details about the employed deterministic fiber tracking algorithm can be found in [3]. Next, we perform a tracking of the same fiber bundle based on the DTI data without tumor. We then apply the total displacement field at time-point i to the these tracked fibers and discard fibers that go through voxels which at time-point i are completely occupied by tumor cells, since we assume that these fibers have been destroyed by the tumor. We consider this second set of fiber bundles $\{T_i\}$ as the ground truth to compare against. We represent the fiber bundles as sets of points and compare them by means of the Hausdorff distance:

$$d_H(F_i, T_i) = \max\left(\max_{x\in F_i}\min_{y\in T_i}\|x-y\|, \max_{y\in T_i}\min_{x\in F_i}\|x-y\|\right). \qquad (14)$$

Further, we analyze the fractional anisotropy of voxels which are pierced by fibers in T_i but not in F_i. We derive the distribution of FA values in these particular voxels and use it to color code the T1 data of a GBM patient. The color coding may be used to evaluate the risk that fiber bundles of interest go through regions infiltrated by the tumor.

3 Results

We simulate an infiltrating tumor near the corticospinal tract of a healthy subject at the level of the corona radiata. The parameters of the DTI acquisition sequence are as follows: resolution = $1.80 \times 1.80 \times 1.98$ mm^3, b value = 1000 s/mm^2, NEX = 2, TR/TE = 12000/84 ms, number of DW images = 62 (2 b_0). Figs. 2(a)-2(f) show tracking results after 0,1,3,5,7, and 9 iterations. Figs. 2(g)-2(i) show details of corresponding tensor fields in proximity of the simulated tumor.

In Fig. 3 we plot the computed Hausdorff distances (see Section 2.4 for details) vs. the volume of the tumor at the various stages of development. In Fig. 4 we present a histogram of FA values in voxels near the tumor where the deflection based FT algorithm failed to reconstruct fibers that were present in the considered ground truth. This histogram is used to generate an appropriate color coding for the GBM segmentation of a patient. This dataset is publicly available from the website [18]. The parameters of the DTI acquisition sequence are as follows: resolution = $1.80 \times 1.80 \times 1.98$ mm^3, b value = 1000 s/mm^2, NEX = 2, TR/TE = 10700/84 ms, number of DW images = 62 (2 b_0). In Fig. 5 voxels whose FA value indicates a high likelihood to contain fibers that may remain undetected by the fiber tracking algorithm are displayed in red, whereas voxels with a lower likelihood are displayed in yellow.

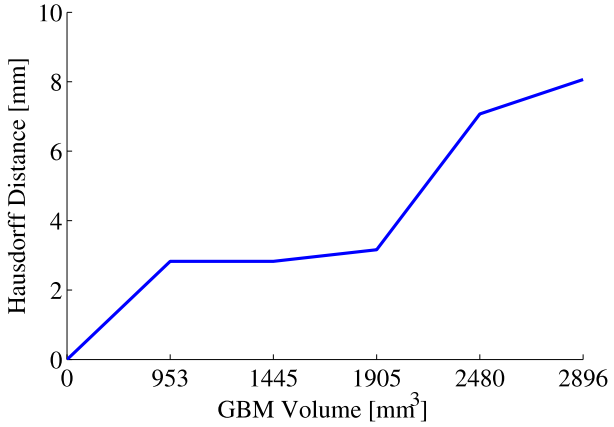

Fig. 3. The computed Hausdorff distances vs. the volume of the simulated GBM.

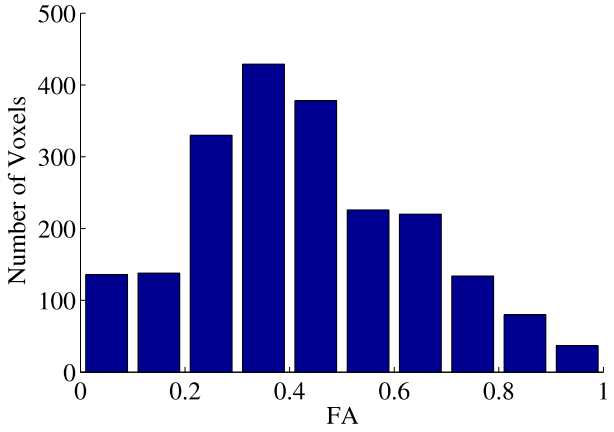

Fig. 4. Histogram of FA values in voxels near the tumor where the deflection based FT algorithm failed to reconstruct fibers that were present in the considered ground truth.

4 Discussion and Conclusions

We have simulated the growth of a GBM starting from imaging data of a healthy volunteer. Compared to the approach presented in [7] we employ the subject's specific DTI data and segmentations of white and grey matter instead of registering to a common atlas. Moreover, we couple the PDEs that describe tumor growth and mass effect by iteratively updating the tumor invaded tensor field. This has allowed us to give a first quantitative indication about the error of FT algorithms in the presence of infiltrated tissue. The data presented in Fig. 3 indicates an error of a few millimeters in the presence of small tumors and of up to 8 mm in the presence of larger tumors. More experiments are needed in order to confirm this initial data. Important parameters which shall be systematically varied in future work include the aggressiveness of the tumor, the specific fiber tract affected by the tumor and the position of the tumor with respect to the tract. We shall also vary the imaging parameters used to acquire the initial data of the healthy volunteer.

The histogram in Fig. 4 indicates that voxels in infiltrated white matter presenting FA values between 0.2 and 0.7 have a high likelihood of containing fibers of interest which the FT algorithm may fail

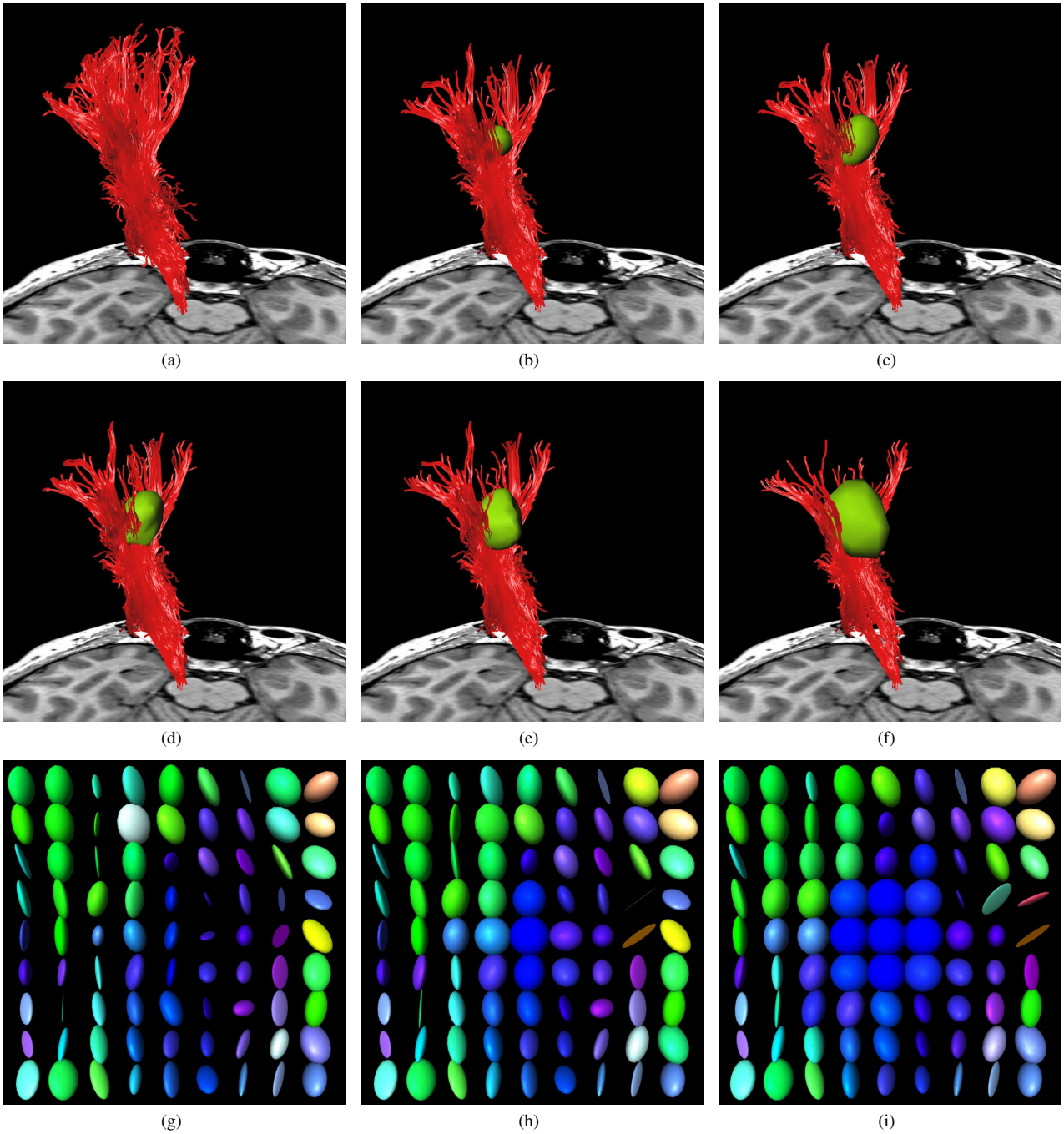

Fig. 2. The red fibers are the result of whole-brain deflection-based FT using a region of interest within the internal capsule to single out the corticospinal tract. The simulated GBM is shown in green, after (a) 0 iterations, volume = 0 mm^3, (b) 1 iterations, volume = 953 mm^3, (c) 3 iterations, volume = 1445 mm^3, (d) 5 iterations, volume = 1905 mm^3, (e) 7 iterations, volume = 2480 mm^3, (f) 9 iterations, volume = 2896 mm^3. (g),(h),(i) show details of corresponding tensor fields in proximity of the simulated tumor after 0,5, and 9 iterations respectively.

to reconstruct. Based upon this result, we have color coded the segmentation of the glioma of a patient, see Fig. 5. Additional experiments shall increase the accuracy of the histogram. An option which we will explore in the future is to visualize this uncertainty in 3D on or around the tracked fibers. In the end, we hope that the presented color coded segmentations may offer clinicians an additional clue about the uncertainty in regions which may potentially contain fiber bundles that need to be preserved.

Acknowledgments

This project was funded in part by the German Research Society (DFG PE199/21-1 & DFG NI568/3-1).

References

[1] I. Amidror. Scattered data interpolation methods for electronic imaging systems: a survey. *J. Elect. Imaging*, 11(2):157–176, 2002.

[2] V. Arsigny, P. Fillard, X. Pennec, and N. Ayache. Log-euclidean metrics for fast and simple calculus on diffusion tensors. *Magn. Reson. Med.*, 56:411–421, 2006.

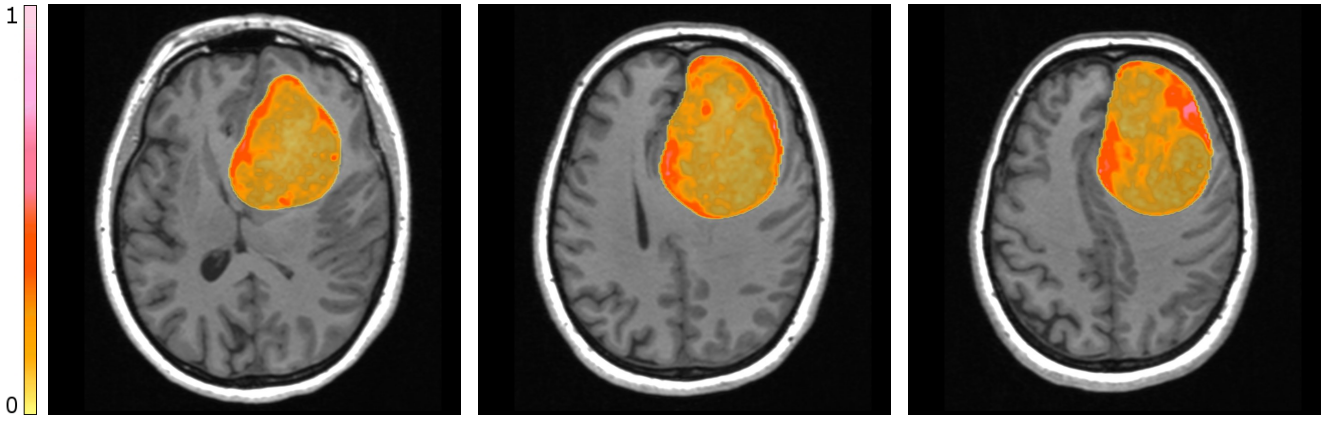

(a) (b) (c)

Fig. 5. (a)-(c) Different slices of the color coded segmentation of a GBM patient. A red color indicates a high risk of fibers which may not be correctly reconstructed by the FT algorithm.

[3] S. Barbieri, M. Bauer, J. Klein, C. Nimsky, and H. Hahn. Segmentation of fiber tracts based on an accuracy analysis on diffusion tensor software phantoms. *NeuroImage*, 55(2):532–544, 2011.

[4] P. Basser. Fiber-tractography via diffusion tensor MRI (DT-MRI). In *Proc. Int. Soc. Magn. Reson. Med.*, 1998.

[5] P. Basser, J. Mattiello, and D. LeBihan. MR diffusion tensor spectroscopy and imaging. *Biophys. J.*, 66(1):259–267, 1994.

[6] Project URL: `http://www.bic.mni.mcgill.ca/brainweb/`.

[7] O. Clatz, P.-Y. Bondiau, H. Delingette, M. Sermesant, S. Warfield, G. Malandain, and N. Ayache. Brain tumor growth and simulation. Technical Report 5187, INRIA, 2004.

[8] T. Conturo, N. Lori, T. Cull, E. Akbudak, A. Snyder, J. Shimony, R. McKinstry, H. Burton, and M. Raichle. Tracking neuronal fiber pathways in the living human brain. In *Proc. Natl. Acad. Sci.*, volume 96, pages 10422–10427, 1999.

[9] V. Cristini, H. Frieboes, X. Li, J. Lowengrub, P. Macklin, S. Sanga, S. Wise, and X. Zheng. *Nonlinear modeling and simulation of tumor growth*. Birkhauser, Boston, 2008.

[10] W. Crum, O. Camara, and D. Hawkes. Methods for inverting dense displacement fields: Evaluation in brain image registration. In *Proc. MICCAI*, pages 900–907, 2007.

[11] G. Cruywagen, D. Woodward, P. Tracqui, G. Bartoo, J. Murray, and E. Alvord. The modelling of diffusive tumors. *J. Biol. Systems*, 3(4):937–945, 1995.

[12] D. Dionysiou, G. Stamatakos, N. Uzunoglu, and K. Nikita. A computer simulation of in vivo tumor growth and response to radiotherapy: New algorithms and parametric results. *Comp. in Biol. and Med.*, 36:448–464, 2006.

[13] E. Fieremans, Y. De Deene, S. Delputte, M. Ozdemir, Y. D'Asseler, J. Vlassenbroeck, K. Deblaere, E. Achten, and I. Lemahieu. Simulation and experimental verification of the diffusion in an anisotropic fiber phantom. *J. Magn. Reson.*, 190(1):189–199, 2008.

[14] J. Francis. The qr transformation, i. *The Computer J.*, 4(3):265–271, 1961.

[15] J. Francis. The qr transformation, ii. *The Comput. J.*, 4(4):332–345, 1962.

[16] C. Gössl, L. Fahrmeir, B. Pütz, L. Auer, and D. Auer. Fiber tracking from DTI using linear state space models: Detectability of the pyramidal tract. *Neuroimage*, 16:378–388, 2002.

[17] H. Hahn, J. Klein, C. Nimsky, J. Rexilius, and H.-O. Peitgen. Uncertainty in diffusion tensor based fibre tracking. *Acta Neurochir. Suppl.*, 98:33–41, 2006.

[18] Image Data, Case 1: `http://viscontest.sdsc.edu/2010/`, 2010.

[19] A. Kansal, S. Torquato, E. Chiocca, and D. T.S. Emergence of a subpopulation in a computational model of tumor growth. *J. Theor. Biol.*, 207:431–441, 2000.

[20] A. Kansal, S. Torquato, G. Harsh, E. Chiocca, and D. T.S. Cellular automaton of idealized brain tumor growth dynamics. *Biosyst.*, 55:119–127, 2000.

[21] A. Kansal, S. Torquato, G. Harsh, E. Chiocca, and D. T.S. Simulated brain tumor growth dynamics using a three-dimensional cellular automaton. *J. Theor. Biol.*, 203:367–382, 2000.

[22] G. Kantor, H. Loiseau, A. Vital, and J. Mazeron. Gross tumor volume (gtv) and clinical target volume (ctv) in adult gliomas. *Cancer Radiother.*, 5(5):571–580, 2001.

[23] M. Kinoshita, K. Yamada, N. Hashimoto, A. Kato, S. Izumoto, T. Baba, M. Maruno, T. Nishimura, and T. Yoshimine. Fiber tracking does not accurately estimate size of fiber bundles in pathological conditions: Initial neurosurgical experience using neuronavigation and subcortical white matter stimulation. *Neuroimage*, 25(2):424–429, 2005.

[24] J. Klein, M. Scholl, A. Koehn, and H. Hahn. Real-time fiber selection using the wii remote. In *Proc. SPIE*, volume 7625, pages 76250N–1–76250N–8, 2010.

[25] V. Kublanovskaya. On some algorithms for the solution of the complete eigenvalue problem. *USSR Comp. Math. and Math. Phys.*, 1(3):637–657, 1961.

[26] X. Li, V. Cristini, Q. Nie, and J. Lowengrub. Nonlinear three-dimensional simulation of solid tumor growth. *Discrete and Continuous Dynamical Systems - Series B*, 7(3):581–604, 2007.

[27] N. Lori, E. Akbudak, J. Shimony, T. Cull, A. Snyder, R. Guillory, and T. Conturo. Diffusion tensor fiber tracking of human brain connectivity: acquisition methods, reliability analysis and biological results. *NMR Biomed.*, 15:493–515, 2002.

[28] S. Mori, B. Crain, V. Chacko, and P. Van Zijl. Three-dimensional tracking of axonal projections in the brain by magnetic resonance imaging. *Ann. Neurol.*, 45(2):265–269, 1999.

[29] J. Neil, S. Shiran, R. McKinstry, G. Schefft, A. Snyder, C. Almli, E. Akbudak, J. Aronovitz, J. Miller, B. Lee, and T. Conturo. Normal brain in human newborns: apparent diffusion coefficient and diffusion anisotropy measured by using diffusion tensor MR imaging. *Radiology*, 209:57–66, 1998.

[30] G. Parker, C. Wheeler-Kingshott, and G. Barker. Estimating distributed anatomical connectivity using fast marching methods and diffusion tensor imaging. *IEEE Trans. Med. Imaging*, 21(5):505–512, 2002.

[31] C. Pierpaoli and P. Basser. Toward a quantitative assessment of diffusion anisotropy. *Magn. Reson. Med.*, 36:893–906, 1996.

[32] S. Price, N. Burnet, T. Donovan, H. Green, A. Pena, N. Antoun, J. Pickard, T. Carpenter, and J. Gillard. Diffusion tensor imaging of brain tumours at 3T: A potential tool for assessing white matter tract invasion? *Clin. Radiol.*, 58(6):455–462, 2003.

[33] W. Slaughter. *The linearized theory of elasticity*. Birkhauser, Boston, 2002.

[34] J.-D. Tournier, F. Calamante, M. King, D. Gadian, and A. Connelly. Limitations and requirements of diffusion tensor fiber tracking: an assessment using simulations. *Magn. Reson. Med.*, 47:701–708, 2002.

[35] P. Tracqui, G. Cruywagen, D. Woodward, G. Bartoo, J. Murray, and E. Alvord. The modelling of diffusive tumors. *J. Biol. Systems*, 3(4):937–945, 1995.